Adaptive Visual Regulation of Wheeled Mobile Robots: a Switching Approach

Qun Lu[1] · Zhijun Li[2] · Li Yu[3] · Chun-Yi Su[4]

Abstract

This paper deals with the visual regulation problem of wheeled mobile robots (WMRs) in the presence of uncalibrated camera-to-robot parameters and unknown image depth. A two-stage controller is designed by using a switching approach. Specifically, in the first stage, an invariant-manifold-based adaptive controller is presented to bring the lateral error and angular error within an arbitrarily small neighborhood of zero; in the second stage, the longitudinal error is regulated by employing a proportional controller. Utilizing the Lyapunov stability analysis, the exponentially bounded stability of the closed-loop system is proved. Both simulation and experimental results are presented to validate the effectiveness of the proposed approach.

Keywords Visual regulation · Wheeled mobile robots · Adaptive control · Invariant manifold

1 Introduction

Visual cameras work as a vision generator and are allowed to conduct non-contact measurements on environments [1]. Owing to the advantages of low cost, high efficiency in information gathering and high reliability, visual cameras have a very wide range of applications in robot systems [2–4], especially in visual servoing which is also called vision-based robot control. Visual servoing uses feedback by gathered information from visual cameras to control the motion of robots [5]. As an important branch of robots, the visual servoing of wheeled mobile robots (WMRs) has been analyzed extensively over the last decades [6–8]. People have studied WMRs with different types of cameras, such as the monocular camera [9], the stereo camera [10] and the omni-directional camera [11]. Meanwhile, different control objectives have been pursued for the WMRs, including the pose stabilization [12], trajectory tracking [13], and the leader-follower formation [14]. From the control point of view, researches have been conducted at the kinematic-level [15] or at the dynamic-level [16]. Based on the control objectives, different control strategies have also been considered, such as the image-based feedback control [17, 18], the position-based feedback control [19] and the 2-1/2-Dimensional (2-1/2-D) hybrid method [20]. At present, most of the the vision sensors used in the industrial field are monocular cameras. Therefore, this paper focuses on the visual servoing with monocular cameras.

The WMR with a monocular camera lacks the 3D model of the scene and the depth information, which makes the stable controller design challenging. Various strategies for the stable control of the monocular-vision-based WMR have been proposed [21–25]. However, it is generally assumed that the camera frame is coincident with the robot frame or the camera-to-robot matrix (extrinsic matrix)

✉ Zhijun Li
  zjli@ieee.org

  Qun Lu
  qun.lu@concordia.ca

  Li Yu
  lyu@zjut.edu.cn

  Chun-Yi Su
  cysu@alcor.concordia.ca

[1] College of Electrical Engineering, Yancheng Institute of Technology, Yancheng 224003, China

[2] Department of Automation, University of Science and Technology of China, Hefei 230000, China

[3] Zhejiang Provincial United Key Laboratory of Embedded Systems, Zhejiang University of Technology, Hangzhou 310023, China

[4] Department of Mechanical, Industrial, and Aerospace Engineering, Concordia University, Montreal, Quebec H3G 1M8, Canada

is well-calibrated, which is not always possible. With the measurement apparatus, the orientation of the camera frame can be adjusted to be the same as that of the robot frame. Whereas, the offset parameters which are related to the translation between the origin of the camera frame and the origin of the robot frame, may not be easy to be set to zero or be measured due to the mechanical structure of the system and the invisible origin of the camera frame. In order to avoid the cumbersome process of extrinsic calibration and improve the flexibility of the WMR systems, a visual servoing method that deals with uncalibrated camera-to-robot parameters is worthy of further investigation. Unfortunately, when considering these unknown parameters, the system model does not satisfy the structural triangularity condition [26, 27], which will bring more challenges for designing the regulation controllers. Thus, much attention has been recently drawn to solve this problem [27–29]. It is noticed that these controllers may not lead to exponential convergence rate [30]. Besides, their control gains may be sensitive to the initial state of the WMR system and the unknown image depth. As a result, parameter tuning methods for these controllers need to be further studied.

The invariant-manifold-based approach is a classical design method for the regulation controllers of the WMRs, which can achieve an exponential convergence rate. Its basic idea is to construct an invariant manifold, on which all the trajectories converge to the origin. Then the invariant manifold is made attractive by employing discontinuous state feedback [30–36]. The exponential convergence rate gives us the motivation to utilize the invariant-manifold-based approach to deal with the visual regulation problem of the WMRs with both uncalibrated extrinsic parameters and unknown image depth. However, the invariant-manifold-based approach is often used in known nonholonomic systems, which needs to be extended to the case with the unknown extrinsic parameters and image depth.

In this paper, we study the visual regulation of a WMR system equipped with a monocular camera and develop an invariant-manifold-based two-stage switching controller. In the first stage, an invariant-manifold-based adaptive controller is designed to bring the lateral and angular errors close to zero, and then the longitudinal error is regulated by resorting to a proportional controller in the second stage. The main contributions of this paper are listed as follows.

1) To solve the visual regulation problem of a WMR in the presence of unknown extrinsic parameters and image depth, we firstly use the feature-point-based pose estimation technique to estimate the relative error between the current and desired configurations of a WMR. Then, we develop a novel adaptive two-stage switching approach to stabilize the visual servoing

system in terms of the relative error. The result also extends the application of the invariant manifold approach.

2) The proposed controller can achieve exponentially bounded stability for the closed-loop visual systems, where the convergence of this approach is faster than that of the most existing approaches as they are time-varying.

3) Compared with the most existing approaches, the control gains of the proposed controller are much easier to be tuned.

The remainder of the paper is organized as follows. The system model is firstly established, and then the control objective is formulated in Section 2. In Section 3, the control development with the stability analysis is presented. The simulation and experimental results are respectively provided in Sections 4 and 5. Some concluding remarks are given in Section 6.

2 Problem Formulation

As a benchmark problem for nonholonomic systems, set-point stabilization of a differential-drive WMR has been widely investigated. The kinematic model of the WMR can be described as

$$\dot{x}_{rw} = v_r \cos\theta_{rw}, \ \dot{y}_{rw} = v_r \sin\theta_{rw}, \ \dot{\theta}_{rw} = \omega_r \qquad (1)$$

As shown in Fig. 1, $(x_{rw}(t), y_{rw}(t))$ is the Cartesian coordinate of the midpoint Q between the two driving wheels in the world frame $\mathcal{F}_w$; θ_{rw} is the angle between the heading direction and the x_w-axis; $v_r(t)$ and $\omega_r(t)$ are the linear and angular velocities of the WMR, respectively. The set-point stabilization problem is how to design control laws for $v_r(t)$ and $\omega_r(t)$ to make the WMR reach a desired configuration $(x_{rw}^*, y_{rw}^*, \theta_{rw}^*)$ from the initial configuration $(x_{rw}^0, y_{rw}^0, \theta_{rw}^0)$. To control the WMR, the current configuration $(x_{rw}(t), y_{rw}(t), \theta_{rw}(t))$ of the WMR needs to be measured in real time via sensors [37–39], such as the inertial measurement unit (IMU), the global positioning system (GPS), etc. Due to the accumulated errors of these sensors, vibration or wheel-slip of the WMR, the measured values for the current configuration may be quite different from their actual values.

In contrast, visual signals can be used to estimate the relative posture between the current and desired configurations of the WMR by using the image pixels of the feature points in the current camera field of view (FOV) and the corresponding image pixels in the desired camera FOV. To achieve this goal, a monocular camera is installed in the WMR, and the system configuration is depicted in Fig. 2. The $\mathcal{F}_r$ and $\mathcal{F}_c$ represent the robot frame and camera frame,

**Fig. 1** Full state regulation problem of a differential-drive WMR
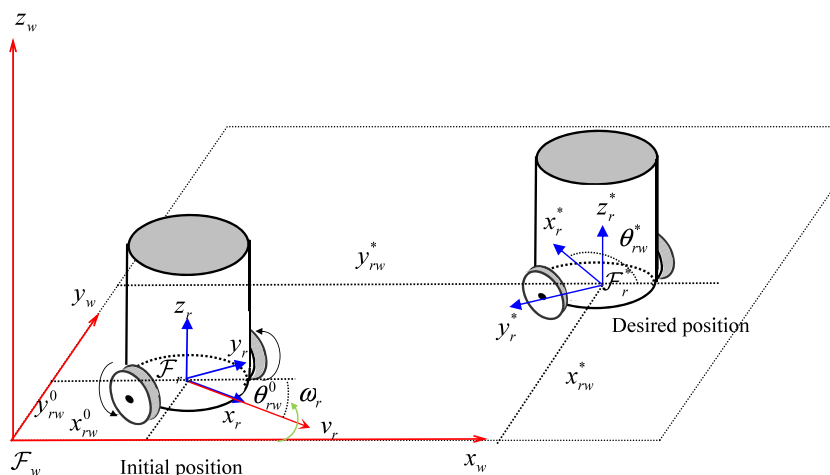
respectively. In $\mathcal{F}_r$, the origin is located at the center of the robot wheel axis, the x-axis x_r is perpendicular to the wheel axis, the y-axis y_r is parallel to the wheel axis, and the z-axis z_r is determined according to the right-hand rule. The orientation of $\mathcal{F}_c$ can be set to be the same as that of $\mathcal{F}_r$. But it may have a different origin as the camera can be installed at any allowable place of the robot shell. The extrinsic parameters which represent the translation between $\mathcal{F}_r$ and $\mathcal{F}_c$ can be described by a vector $[L, D, H]^{\mathrm{T}} \in \mathbb{R}^3$, where L, D and H are the coordinates of $\mathcal{F}_c$'s origin along x_r, y_r and z_r, respectively. As shown in Fig. 2, the orthogonal coordinate systems $\mathcal{F}_r^*$ and $\mathcal{F}_c^*$ are introduced to indicate the desired configurations of the WMR and the camera.

Remark 1 The Eq. 1 is valid only if the mobile base of the WMR satisfies the "pure rolling without slipping" condition. However, infrequent mild slipping is allowed

in this paper, since the scaled relative errors can still be estimated with the vision-based pose estimation techniques. Frequent slipping will cause the feature points to escape from the camera FOV, and if mild slipping happens frequently, then Eq. 1 is invalid. Therefore, serious or frequent mild slipping will not be considered in this paper.

Remark 2 Figure 3 depicts the WMR testbed where the back plane and bottom plane of the camera can be adjust to be parallel to the plane 1 and 2 of the WMR shell with the measurement apparatus, such as the dial indicator and level. In other words, considering the relationship between the main part of the WMR and its shell, the orientation of $\mathcal{F}_c$ can be adjusted to be coincident with that of $\mathcal{F}_r$. However, limited by the mechanical structure of the WMR itself, the camera cannot be installed in the origin of $\mathcal{F}_r$. Moreover,

Fig. 2 Vision-based regulation problem of a differential-drive WMR
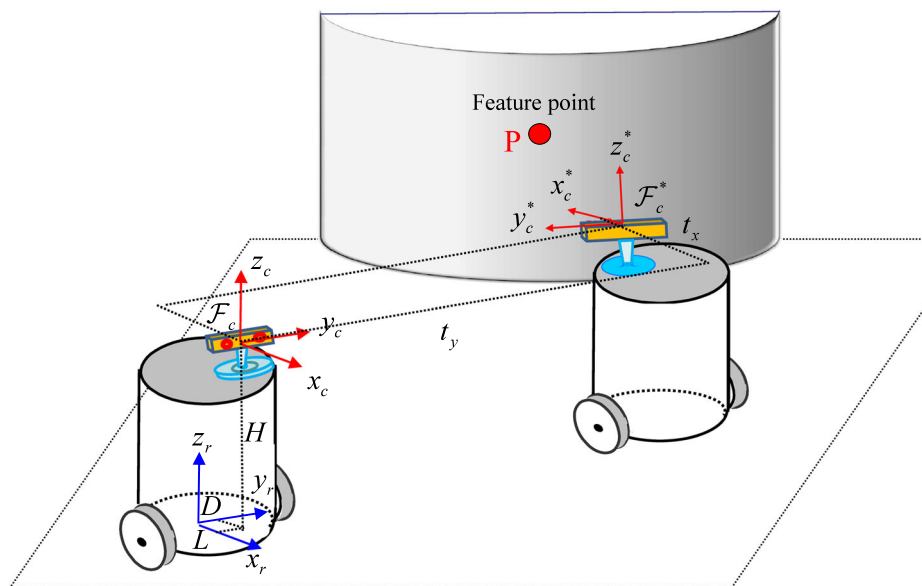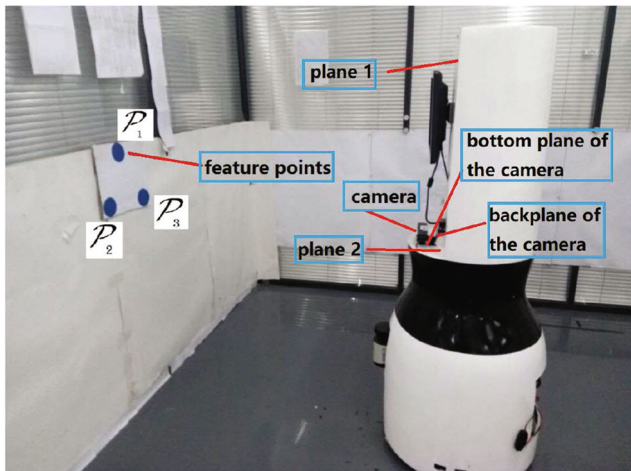
Fig. 3 Experimental setup

the extrinsic parameters are difficult to be measured as the origin of the camera frame is invisible and the main part of the WMR is encapsulated by the shell. Therefore, it is reasonable to assume that L, D, H are unknown.

2.1 The Feature-Points-Based Pose Estimation

Suppose there are three static feature points $\mathcal{P}_i$ ($i = 1, 2, 3$) in the scene, and their 3D coordinates $P_i(t)$, $P_i^* \in \mathbb{R}^3$ in the frames $\mathcal{F}_c$ and $\mathcal{F}_c^*$ are defined by

$$P_i = [X_i(t), Y_i(t), Z_i(t)]^{\mathrm{T}}, \quad P_i^* = [X_i^*, Y_i^*, Z_i^*]^{\mathrm{T}} \quad (2)$$

Denote the corresponding image pixel coordinates by

$$p_i = [1, u_i(t), v_i(t)]^{\mathrm{T}}, \quad p_i^* = [1, u_i^*, v_i^*]^{\mathrm{T}} \quad (3)$$

It is obvious that the image coordinates are associated with the camera coordinates according to the pinhole camera model in the following

$$p_i = \frac{1}{X_i} K_{int} P_i, \quad p_i^* = \frac{1}{X_i^*} K_{int} P_i^* \quad (4)$$

where invertible matrix $K_{int} \in \mathbb{R}^{3 \times 3}$ indicates the intrinsic camera matrix, and it can be determined by following the procedures of the camera calibration techniques [40]. For the sake of subsequent discussion, the normalized image coordinates are introduced

$$m_i = [1, y_i(t), z_i(t)]^{\mathrm{T}} = \frac{1}{X_i} P_i, \quad m_i^* = [1, y_i^*, z_i^*]^{\mathrm{T}} = \frac{1}{X_i^*} P_i^* \quad (5)$$

On the basis of Eqs. 3–5, it is obvious that $m_i(t)$ and m_i^* can be given as follows

$$m_i = K_{int}^{-1} p_i, \quad m_i^* = K_{int}^{-1} p_i^* \quad (6)$$

As the camera is installed rigidly at the WMR and the WMR's motion stays in the $x_w y_w$ plane, the relative posture

between the current and desired configurations of the WMR can be described by $(t_x(t), t_y(t), \theta(t))$, where $t_x(t), t_y(t) \in \mathbb{R}$ denote the translation along x_c-axis and y_c-axis between $\mathcal{F}_c$ and $\mathcal{F}_c^*$, respectively; $\theta(t) \in (-\pi, \pi]$ represents the rotational angle between $\mathcal{F}_r$ and $\mathcal{F}_r^*$, which is also called angular error. According to the definitions of $t_x(t), t_y(t)$ and $\theta(t)$, one has

$$\begin{cases} \theta = \theta_{rw} - \theta_{rw}^* \\ \begin{bmatrix} t_x \\ t_y \end{bmatrix} = \begin{bmatrix} \cos\theta_{rw} & \sin\theta_{rw} \\ -\sin\theta_{rw} & \cos\theta_{rw} \end{bmatrix} \begin{bmatrix} x_{rw} - x_{rw}^* \\ y_{rw} - y_{rw}^* \end{bmatrix} \end{cases} \quad (7)$$

From Eq. 7, we know that (θ, t_y, t_x) can be regarded as a regulation error. However, t_x and t_y cannot be computed through 2-D images with an unknown 3-D scene model. Therefore, in the visual servoing process, we will use an equivalent regulation error $e = [e_0, e_1, e_2]^{\mathrm{T}}$, which are defined as

$$e_0(t) = \theta, \quad e_1(t) = \frac{t_y}{Z_i^*}, \quad e_2(t) = \frac{t_x}{Z_i^*} \quad (8)$$

Since Z_i^* will not be changed due to the WMR moving in the horizon plane x_w-y_w, $(\theta(t), t_y(t), t_x(t))$ and $(e_0(t), e_1(t), e_2(t))$ are equivalent. Moreover, $e_1(t)$ and $e_2(t)$ are also called the lateral error and longitudinal error, respectively.

It is clear that $\theta(t)$ is equal to the angle between $\mathcal{F}_c$ and $\mathcal{F}_c^*$, and $t_x(t)$ and $t_y(t)$ are equal to the translation along x_c-axis and y_c-axis between $\mathcal{F}_c$ and $\mathcal{F}_c^*$. Define $R(\theta(t))$ as the rotation matrix specifying the orientation of $\mathcal{F}_c^*$ with respect to $\mathcal{F}_c$, and then we can obtain

$$P_i = R P_i^* + T \quad (9)$$

where $R = \begin{bmatrix} \cos\theta & -\sin\theta & 0 \\ \sin\theta & \cos\theta & 0 \\ 0 & 0 & 1 \end{bmatrix}$, $T = \begin{bmatrix} t_x \\ t_y \\ 0 \end{bmatrix}$.

From Eqs. 2 and 9, the following results can be easily found

$$\begin{cases} \frac{Y_i}{X_i} = \frac{X_i^* \sin\theta + Y_i^* \cos\theta + t_y}{X_i^* \cos\theta - Y_i^* \sin\theta + t_x}, \\ \frac{Z_i}{X_i} = \frac{Z_i^*}{X_i^* \cos\theta - Y_i^* \sin\theta + t_x}. \end{cases} \quad (10)$$

Dividing top and bottom on the right side of Eq. 10 by X_i^* and using Eq. 5, then Eq. 10 can be rewritten as

$$\begin{cases} y_i = \frac{\sin\theta + y_i^* \cos\theta + \frac{t_y}{X_i^*}}{\cos\theta - y_i^* \sin\theta + \frac{t_x}{X_i^*}} \\ z_i = \frac{z_i^*}{\cos\theta - y_i^* \sin\theta + \frac{t_x}{X_i^*}} \end{cases} \quad (11)$$

We can choose a set of arbitrary feature points such that $y_i(t) \neq y_j(t)$ and $z_i(t) \neq 0$ ($i, j = 1, 2, 3$). Then based on Eq. 11, we can get the estimation of θ by using the

least-square method. Once $\theta(t)$ is obtained, $e_1(t)$ and $e_2(t)$ can be computed directly from Eqs. 5 and that

$$\begin{bmatrix} e_1 \\ e_2 \end{bmatrix} = \begin{bmatrix} \frac{y_i}{z_i} \\ \frac{1}{z_i} \end{bmatrix} - \begin{bmatrix} \cos\theta & \sin\theta \\ -\sin\theta & \cos\theta \end{bmatrix} \begin{bmatrix} \frac{y_i^*}{z_i^*} \\ \frac{1}{z_i^*} \end{bmatrix} \tag{12}$$

Remark 3 As $e_1(t)$ and $e_2(t)$ depend on Z_i^*, different feature points will generate different error signals. In practice, only one feature point is selected for the controller design and in this paper we suppose that we use the ith feature point. Moreover, according to the feature-point-based pose estimation technique, the number of the feature pints in the camera FOV is at least 2, and for the specific feature point, its $e_0(t)$, $e_1(t)$, $e_2(t)$ can be computed directly or reconstructed from those of the other feature points.

2.2 Model Development

When the WMR is moving, the position of $\mathcal{P}_i$ in $\mathcal{F}_r$, denoted as $P_{i,r} = [X_{i,r}(t), Y_{i,r}(t), Z_{i,r}(t)]^T$, is also changing due to the movement of $\mathcal{F}_r$, and the dynamic equation of $P_{i,r}(t)$ can be described as [21]

$$\dot{X}_{i,r} = \omega Y_{i,r} - v_r, \quad \dot{Y}_{i,r} = -\omega_r X_{i,r} \tag{13}$$

As shown in Fig. 2, the relationship between $P_i(t)$ and $P_{i,r}(t)$ is described as

$$X_{i,r} = X_i + L, \quad Y_{i,r} = Y_i + D \tag{14}$$

From Eq. 1 and the definition of $e_0(t)$, we can obtain

$$\dot{e}_0 = \omega_r \tag{15}$$

Due to the planar motion of the WMR, the equation $Z_i = Z_i^*$ always holds. Taking the time derivatives of Eqs. 12 and 14, and then inserting Eqs. 13–15 into the resultant equations, we can get the dynamic equations of $e_1(t)$ and $e_2(t)$

$$\dot{e}_1 = -e_2\omega_r - \rho\omega_r \tag{16}$$

$$\dot{e}_2 = e_1\omega_r + \frac{D}{d^*}\omega_r - \frac{1}{d^*}v_r \tag{17}$$

where $d^* = Z_i^*$, $\rho = \frac{L}{d^*}$.

The control objective in this paper is to design a control law (ω_r, v_r) for system (15)–(17) such that

$$\lim_{t \to \infty} |e_0(t)| \leq \tau_{e0}, \ \lim_{t \to \infty} |e_1(t)| \leq \tau_{e1}, \ \lim_{t \to \infty} |e_2(t)| \leq \tau_{e2} \tag{18}$$

where τ_{e0}, τ_{e1}, τ_{e2} are arbitrary small positive thresholds.

3 Controller Design

The classical invariant-mainfold-based approach is often used to stabilize the deterministic nonholonomic systems.

However, it cannot be directly utilized to stabilize the unknown system (15)–(17). In [30], backstepping technique and invariant manifold were combined to stabilize the WMRs with matched uncertainties, where the input disturbances were estimated online. However, the subsystem (16) involves the unknown parameters, which is different from [30]. $v_r(t)$ and the unknown d^* are coupled in the subsystem (17), and when the method proposed in [36] is applied to the system (15)–(17), the resulting system cannot be written in the form of linear system. Hence, the stability cannot be guaranteed by linear system theory. As a result, the method proposed in [36] is not applicable to the system (15)–(17). In this section, an adaptive two-stage controller will be designed to achieve the control objective (18).

Before proceeding to the controller design, the following assumption is presented as follows.

Assumption 1 The initial states of $e_0(t)$ and $e_1(t)$ need to satisfy one of the two following conditions:

C1) $$|e_0(0)| > \tau_{e0} \tag{19}$$

C2) $$|e_0(0)| \leq \tau_{e0}, \ |e_1(0)| \leq \tau_{e1} \tag{20}$$

Remark 4 If the initial states do not meet Assumption 1, then by applying some control laws, such as $\omega_r = -k_s(e_0 - \text{sgn}(e_0(0))c_s)$, $v_r = 0$ with k_s, $c_s > \tau_{e0}$ are positive constants, for a period of time, the system can be driven away from $|e_0| \leq \tau_{e0}$. Thus, condition C1 will become true and Assumption 1 will be satisfied.

Under Assumption 1, a two-stage controller is proposed for the system (15)–(17) as follows.

1) Stage I: Design $\omega_r(t)$ and $v_r(t)$ to make the angular error and the lateral error bounded by their thresholds in a finite time, namely, $\exists T_1 > 0, \forall t \geq T_1, |e_0(t)| \leq \tau_{e0}$ and $|e_1(t)| \leq \tau_{e1}$ are satisfied;
2) Stage II: Design $\omega_r(t)$ and $v_r(t)$ to make the longitudinal error bounded by its threshold in a finite time, namely, $\exists T_2 > T_1, \forall t \geq T_2, |e_2(t)| \leq \tau_{e2}$ is satisfied.

Remark 5 If the condition C1 in Assumption 1 is satisfied, then the two-stage controller needs to be implemented step by step. Else if the condition C2 in Assumption 1 is satisfied, then the controller directly switches to Stage II.

3.1 Controller Design in Stage I

Inspired by the invariant-manifold-based approach for the full state regulation problem of the WMRs [33], the following auxiliary signal $\hat{S}(t) \in \mathbb{R}$ is introduced:

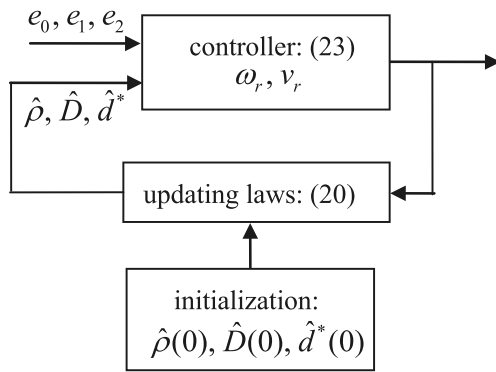$$\hat{S} = e_1 + \frac{k_0}{K_b}e_0e_2 + \hat{\rho}e_0 \tag{21}$$

Fig. 4 The flowchart of the visual regulation controller in Stage I

where $\hat{\rho}(t) \in \mathbb{R}$ is the online estimation of the unknown constant ρ, the constants $k_0 \in \mathbb{R}^+$, $k_1 \in \mathbb{R}^+$, $K_b = k_0 + k_1$ are control gains, and $k_0 \neq k_1$.

For the sake of subsequent discussion, the parameter estimation errors $\tilde{d}^*(t) \in \mathbb{R}$, $\tilde{D}(t) \in \mathbb{R}$ and $\tilde{\rho}(t) \in \mathbb{R}$ are defined as:

$$\tilde{d}^* = d^* - \hat{d}^*, \quad \tilde{D} = D - \hat{D}, \quad \tilde{\rho} = \rho - \hat{\rho} \tag{22}$$

where $\hat{d}^*(t) \in \mathbb{R}$ and $\hat{D}(t) \in \mathbb{R}$ are estimates of d^* and D, respectively. If the condition C1 in Assumption 1 is satisfied, then according to the subsequent stability analysis, the parameter updating laws can be designed as follows:

$$\dot{\hat{\rho}} = \Gamma_1 k_0 \Upsilon, \quad \dot{\hat{\xi}} = \Gamma_2 \Psi \tag{23}$$

where $\Upsilon = \frac{\hat{S}}{e_0}$; $\hat{\xi}(t) \in \mathbb{R}^2$ is the online estimation of $\xi = [D, d^*]^{\mathrm{T}}$; $\Gamma_1 \in \mathbb{R}$ is a positive constant scalar; and $\Gamma_2 \in \mathbb{R}^{2 \times 2}$ is a positive constant diagonal matrix. $[\Psi_1(t), \Psi_2(t)]^{\mathrm{T}} \in \mathbb{R}^2$ are defined as
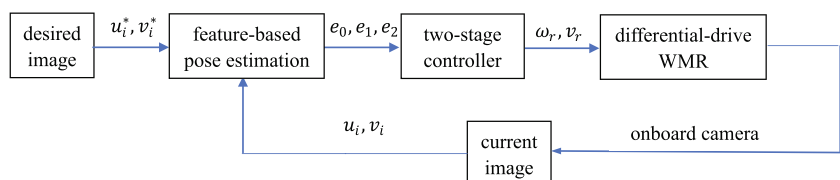
$$\Psi_1 = \mathrm{sgn}(d^*) \left(\frac{k_0}{K_b} \Upsilon + K_1 e_2 \right) \omega_r \tag{24}$$

$$\Psi_2 = \mathrm{sgn}(d^*) \left(K_1 e_2 + \frac{k_0}{K_b} \Upsilon \right) (\omega_r e_1 + k_2 e_2)$$

$$- \mathrm{sgn}(d^*) \left(\frac{k_0 k_4}{K_b} \Upsilon^2 - K_1^2 K_2 e_2^2 \right) \tag{25}$$

where $K_1 \in \mathbb{R}^+$, $k_2 \in \mathbb{R}^-$, $K_2 = \frac{K_b k_2}{k_0} \in \mathbb{R}$, $\mathrm{sgn}(x)$ is a sign function. The adaptive controllers are constructed as follows:

$$\omega_r = -k_0 e_0, \quad v_r = (\hat{d}^* e_1 + \hat{D}) \omega_r - \hat{d}^* (k_2 \Upsilon - k_1 e_2) + \chi \tag{26}$$

Fig. 5 Diagram of visual servoing system

where the auxiliary signal $\chi(t) \in \mathbb{R}$ is defined as

$$\chi = \hat{d}^* K_1 K_2 e_2 \tag{27}$$

The flow chart of Stage I is sketched in Fig. 4 and the control gains satisfy the following conditions

$$K_3 > 0, \quad K_b + k_2 < 0, \quad \frac{k_2}{K_b} + \Gamma_1 < -1 \tag{28}$$

where $K_3 = k_1 + K_1 K_2$ is a constant scalar. After substituting Eqs. 26 and 27 into Eq. 15–17, we can get the closed-loop system

$$\begin{cases} \dot{e}_0 = -k_0 e_0 \\ \dot{e}_1 = (e_2 + \rho) k_0 e_0 \\ \dot{e}_2 = -\dfrac{k_0 e_0 (\tilde{d}^* e_1 + \tilde{D})}{d^*} + \dfrac{\hat{d}^*}{d^*} (k_2 \Upsilon - K_3 e_2) \end{cases} \tag{29}$$

Theorem 1 *Considering system* (15)–(17), *if conditions* (19) *and* (28) *are satisfied, the control laws* (26) *and the parameter updating laws* (23) *ensure that*

1) *the regulation error $e(t)$ converges to zero and the control input as well as the estimated parameters are all bounded;*

2) *the angular error $e_0(t)$ and the lateral error $e_1(t)$ are bounded by their thresholds in a finite time, i.e., for any $\tau_{e0} > 0$ and $\tau_{e1} > 0$, there always existing $T_1 > 0$, such that $\forall t \geq T_1$, $|e_0(t)| \leq \tau_{e0}$ and $|e_1(t)| \leq \tau_{e1}$.*

Proof 1) It can be inferred from Eq. 29 that $e_0(t) \in \mathcal{L}_\infty$ and e_0 decays exponentially to zero, which implies that

$$\lim_{t \to \infty} e_0(t) = 0 \tag{30}$$

Moreover, as the condition (19) is satisfied, $e_0(t)$ will converge to and never be zero. Define the following candidate Lyapunov function as

$$V(t) = \frac{1}{2}|d^*|K_1 e_2^2 + \frac{1}{2}|d^*|\Upsilon^2 + \frac{1}{2}|d^*|\Gamma_1^{-1}\tilde{\rho}^2 + \frac{1}{2}\tilde{\xi}^{\mathrm{T}}\Gamma_2^{-1}\tilde{\xi} \tag{31}$$

For convenience, denote

$$V_1(t) = \frac{1}{2}|d^*|K_1 e_2^2 \qquad V_2(t) = \frac{1}{2}|d^*|\Upsilon^2$$

$$V_3(t) = \frac{1}{2}|d^*|\Gamma_1^{-1}\tilde{\rho}^2 \qquad V_4(t) = \frac{1}{2}\tilde{\xi}^{\mathrm{T}}\Gamma_2^{-1}\tilde{\xi} \tag{32}$$

Table 1 A new two-stage control scheme

Stage	System model	Goal	Controller
Stage I	System (15)–(17)	$\|e_0\| \le \tau_{e0}, \|e_1\| \le \tau_{e1}$	ω_r, v_r: (26)
Stage II	System (45)	$\|e_2\| \le \tau_{e2}$	$\omega_r = 0, v_r$: (46)

We rewrite the subsystem of Eq. 29 in the form of parameter estimation errors

$$\dot{e}_2 = k_2\Upsilon - K_3 e_2 + \frac{\tilde{D}}{d^*}\omega_r + \frac{\tilde{d}^*}{d^*}(e_1\omega_r - k_2\Upsilon + K_3 e_2) \tag{33}$$

Taking the time derivative of $\Upsilon(t)$ and substituting Eqs. 23, 29, and 33 into the resultant expression, we obtain

$$\dot{\Upsilon} = \frac{\dot{e}_1 e_0 - e_1 \dot{e}_0}{e_0^2} + \frac{k_0}{K_b}\dot{e}_2 + \dot{\hat{\rho}}$$

$$= \lambda_1 \Upsilon + k_0 \tilde{\rho} + \frac{k_0}{K_b}\left(\frac{\tilde{d}^* e_1 + \tilde{D}}{d^*}\omega_r - K_1 K_2 e_2\right)$$

$$- \frac{\tilde{d}^*}{d^*}(k_2\Upsilon - K_3 e_2) \tag{34}$$

Fig. 6 Simulation results with the proposed controller: **a** System errors e; **b** Image trajectories of $\mathcal{P}_i$; **c** Online estimation of d^*, ρ, D; **d** Control inputs
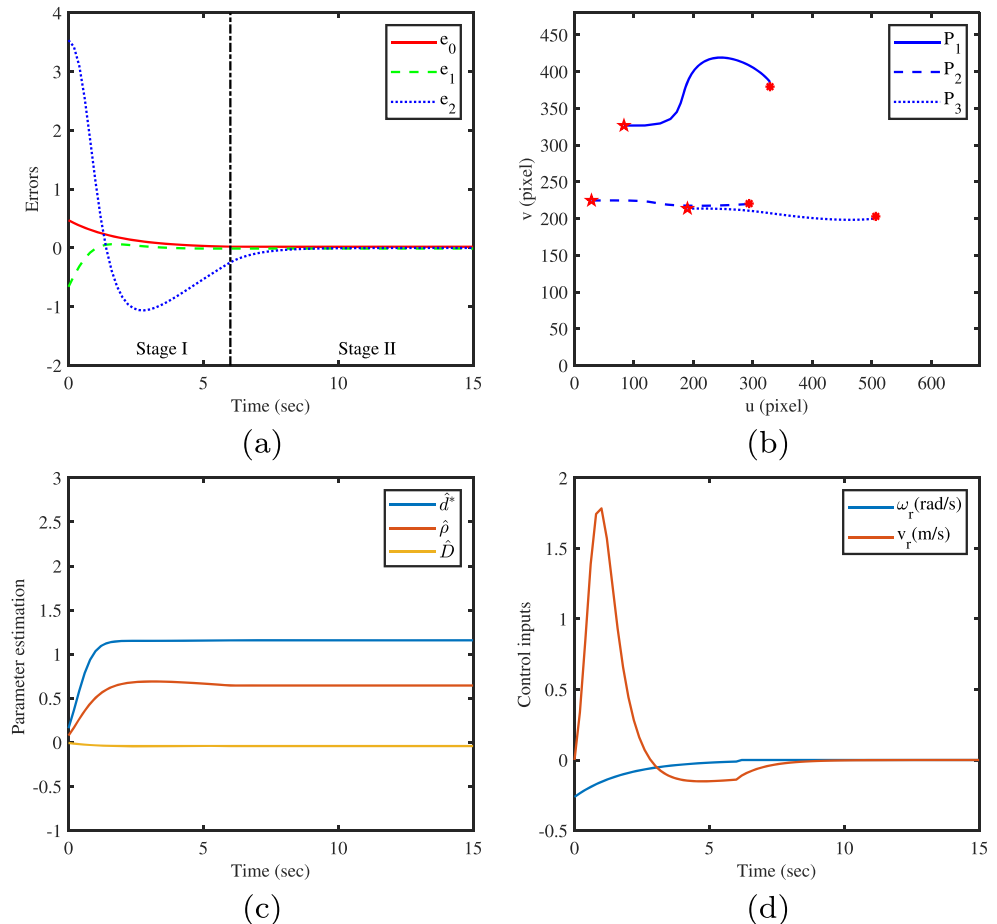
where $\lambda_1 = k_0\left(\frac{k_4}{K_b} + \Gamma_1 + 1\right)$ is a constant scalar. Taking the time derivative of each item in Eq. 32 and substituting Eqs. 23, 33 and 34 into the corresponding resultant expression, we obtain

$$\dot{V}_1 = |d^*|K_1 e_2 (k_2\Upsilon - K_3 e_2) + \text{sgn}(d^*)\tilde{D}K_1 e_2\omega_r$$

$$+ \text{sgn}(d^*)\tilde{d}^* K_1 e_2 (e_1\omega_r - k_2\Upsilon + K_3 e_2) \tag{35}$$

$$\dot{V}_2 = |d^*|\lambda_1\Upsilon^2 + |d^*|k_0\tilde{\rho}\Upsilon - |d^*|\frac{\tilde{d}^*}{d^*}(k_2 Y - K_3 e_2)\Upsilon$$

$$+ |d^*|\frac{k_0}{K_b}\left(\frac{\tilde{d}^* e_1 + \tilde{D}}{d^*}\omega_r - K_1 K_2 e_2\right)\Upsilon \tag{36}$$

$$\dot{V}_3 = -|d^*|k_0\Upsilon\tilde{\rho} \tag{37}$$

$$\dot{V}_4 = -\text{sgn}(d^*)\tilde{d}^*\left(K_1 e_2 + \frac{k_0}{K_b}\Upsilon\right)(\omega_r e_1 + k_1 e_2)$$

$$+ \text{sgn}(d^*)\tilde{d}^*\left(\frac{k_0 k_2}{K_b}\Upsilon^2 - K_1^2 K_2 e_2^2\right)$$

$$- \text{sgn}(d^*)\tilde{D}\left(\frac{k_0}{K_b}\Upsilon + K_1 e_2\right)\omega_r \tag{38}$$

Table 2 Comparative study

Cases	System parameters
The original setting	$e(0) = [0.524, -0.866, 3.5]^T$, $d^* = 0.5$ m, $L = 0.2$ m, $D = 0.1$ m;
Case 1: different $e(0)$	$e(0) = [0.449, -0.8, 3]^T$, $d^* = 0.5$ m, $L = 0.2$ m, $D = 0.1$ m;
Case 2: different d^*	$e(0) = [0.524, -0.866, 3.5]^T$, $d^* = 0.4$ m, $L = 0.2$ m, $D = 0.1$ m;
Case 3: different L	$e(0) = [0.524, -0.866, 3.5]^T$, $d^* = 0.5$ m, $L = 0.3$ m, $D = 0.1$ m;
Case 4: different D	$e(0) = [0.524, -0.866, 3.5]^T$, $d^* = 0.5$ m, $L = 0.2$ m, $D = 0.2$ m.

According to Eqs. 35–38, we have

$$\dot{V} = |d^*|\lambda_1 \Upsilon^2 + |d^*|\lambda_2 e_2^2 \qquad (39)$$

where $\lambda_2 = -K_1 K_3$ is a constant scalar.

If $K_1 > 0$, $K_3 > 0$ and $\frac{k_2}{K_b} + \Gamma_1 < -1$, then $\lambda_1, \lambda_2 < 0$, so $V(t) \geq 0$, $\dot{V}(t) \leq 0$. From the Lyapunov stability theory, we have $\Upsilon(t), e_2(t), \tilde{\rho}(t), \tilde{\xi}(t) \in \mathcal{L}_\infty$. Based on the facts of $e_0(t), e_2(t), \Upsilon(t) \in \mathcal{L}_\infty$, we can infer that $\hat{\rho}(t) = \rho - \tilde{\rho}(t) \in \mathcal{L}_\infty$. From Eq. 21, we know that $\frac{e_1(t)}{e_0(t)} \in \mathcal{L}_\infty$, and then $e_1(t) \in \mathcal{L}_\infty$. Then it can be obtained from Eqs. 22, 24, 25 and 27 that $\hat{\xi}(t), \Psi(t), \chi(t) \in \mathcal{L}_\infty$. Similarly, it follows from Eq. 26 that $\omega_r(t), v_r(t) \in \mathcal{L}_\infty$.

To show that $\lim_{t\to\infty} e_1(t) = 0$ and $\lim_{t\to\infty} e_2(t) = 0$, a scalar function $\vartheta(t)$ is defined as

$$\vartheta = -|d^*|\lambda_1 \Upsilon^2 - |d^*|\lambda_2 e_2^2 \geq 0 \qquad (40)$$

Taking the time derivative of $\vartheta(t)$, we get

$$\dot{\vartheta} = -2|d^*|\lambda_1 \Upsilon \dot{\Upsilon} - 2|d^*|\lambda_2 e_2 \dot{e}_2 \qquad (41)$$

From Eqs. 33 and 34, we can get $\dot{e}_2(t), \dot{\Upsilon}(t) \in \mathcal{L}_\infty$. Hence, $\vartheta(t), \dot{\vartheta}(t) \in \mathcal{L}_\infty$, which implies that ϑ is uniformly continuous. Based on the facts of $V(t) \geq 0$, $\dot{V}(t) \leq 0$, and $\vartheta(t) = -\dot{V}(t)$, we can conclude that $\vartheta(t) \in \mathcal{L}_2$. According to the extended Barbalat's

Fig. 7 Simulation results with the proposed controller: **a** Different initial errors $e(0)$; **b** Different d^*; **c** Different L; **d** Different D

(a)

(b)

(c)

(d)
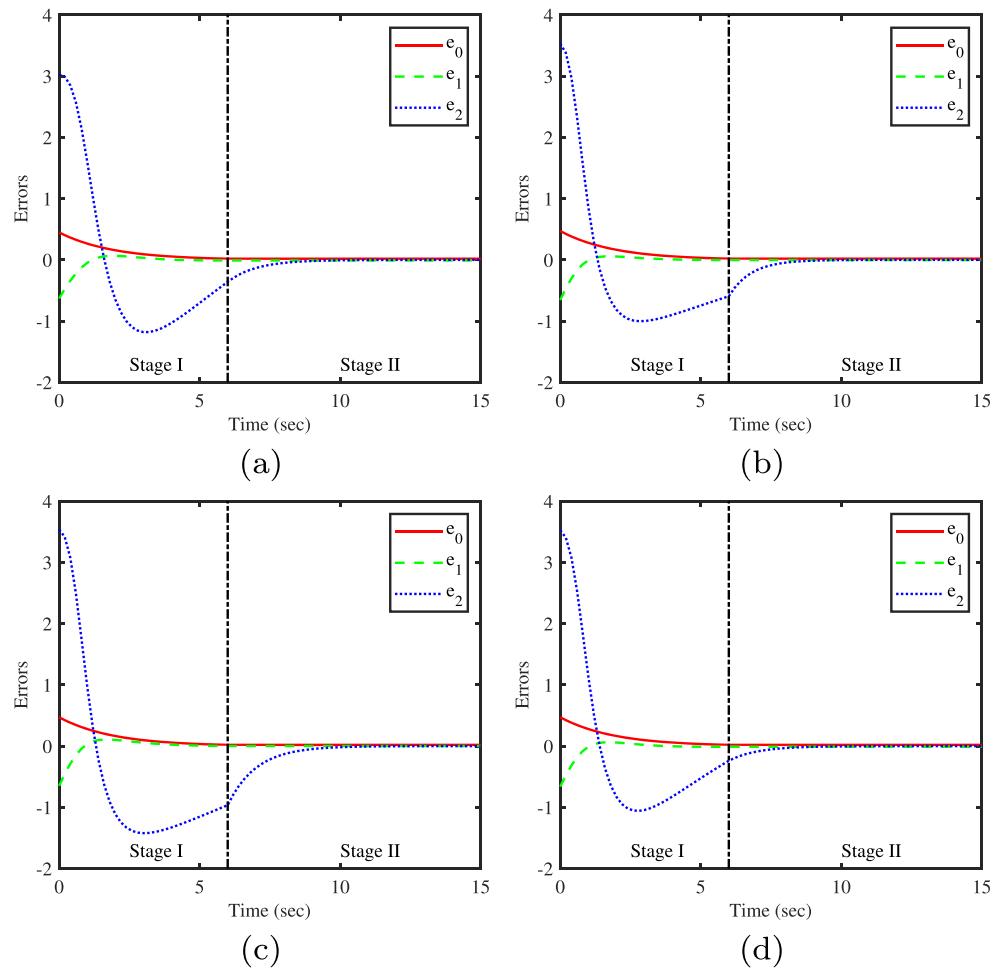
lemma [41], we have $\lim\limits_{t\to\infty} \vartheta(t) = 0$. Then, it follows from Eq. 41 that

$$\lim_{t\to\infty} e_2(t) = 0, \quad \lim_{t\to\infty} \Upsilon(t) = 0 \tag{42}$$

From Eqs. 23 and 42, we know that $\hat{\rho}(t)$ will converge to a constant C when $t \to \infty$. Then, from $\Upsilon(t) = \frac{e_1}{e_0} + \frac{k_0 e_2}{K_b} + \hat{\rho}$, $e_2 \to 0$, and $e_0 \to 0$, we have

$$\lim_{t\to\infty} \frac{e_1(t)}{e_0(t)} = -\lim_{t\to\infty} \hat{\rho}(t) = -C, \quad \lim_{t\to\infty} e_1(t) = 0 \tag{43}$$

By combining Eqs. 30, 42, and 43, we obtain

$$\lim_{t\to\infty} e_0(t) = 0, \quad \lim_{t\to\infty} e_1(t) = 0, \quad \lim_{t\to\infty} e_2(t) = 0 \tag{44}$$

and the control input $v_r(t), \omega_r(t)$ as well as all estimated parameters $\hat{\rho}(t), \hat{D}(t), \hat{d}^*(t)$ are bounded.

2) As $e_0(t)$ decays exponentially to zero and $\frac{e_1(t)}{e_0(t)}$ converges to the constant $-C$, $e_1(t)$ also decays exponentially to zero. From the (ε, δ)-definition of limit we know that there always exists $T_1 > 0, \forall t \geq T_1$, such that $|e_0(t)| \leq \tau_{e0}$ and $|e_1(t)| \leq \tau_{e1}$. The proof is thus completed.

$\square$

From Theorem 1 we know that $\forall t \geq T_1, |e_0(t)| \leq \tau_{e0}$ and $|e_1(t)| \leq \tau_{e1}$. Since τ_{e0}, τ_{e1} are arbitrary small constants, $e_0(t), e_1(t)$ do not need to be regulated anymore when $t \geq T_1$. Although $\lim\limits_{t\to\infty} e_2(t) = 0$, we cannot guarantee $|e_2(t)| \leq \tau_{e2}$ when $t > T_1$. Thus, we turn to the regulation of $e_2(t)$ in Stage II.

3.2 Controller Design in Stage II

Inspired by [27], when $|e_0(t)| \leq \tau_{e0}$ and $|e_1(t)| \leq \tau_{e1}$, we do not want to change e_0 and e_1 anymore. To achieve this goal, the angular velocity is designed as $\omega_r(t) = 0$ and by substituting it into the system (15)–(17), we get

$$\dot{e}_0 = 0, \quad \dot{e}_1 = 0, \quad \dot{e}_2 = -\frac{v_r}{d^*} \tag{45}$$

From Eq. 45 we know that e_0 and e_1 will not be changed. To regulate $e_2(t)$, a proportional controller is designed as follows.

$$v_r = k_3 e_2 \tag{46}$$

where $k_3 \in \mathbb{R}$ represents a control gain, and it has the same sign as d^*. By linear system theory, the longitudinal error $e_2(t)$ will decay exponentially to zero. Similarly, from the (ε, δ)-definition of limit we know that there always exists $T_2 > T_1$, such that $\forall t \geq T_2$, we have $|e_2(t)| \leq \tau_{e2}$.

The diagram of the visual servoing system is depicted in Fig. 5 and the whole process of the proposed two-stage controller is summarized at Table 1. As $\tau_{e0}, \tau_{e1}, \tau_{e2}$
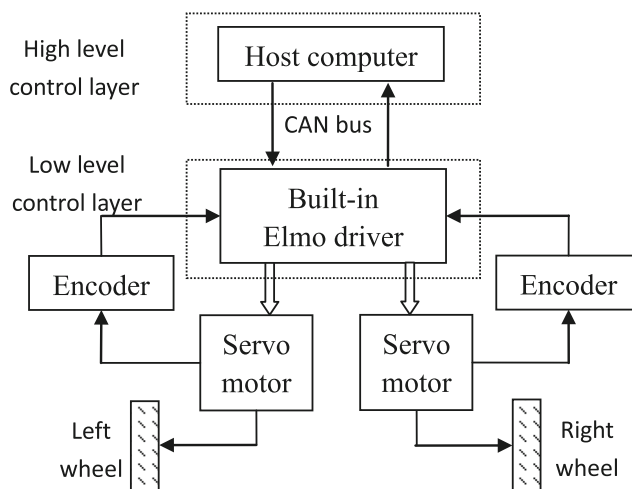

Fig. 8 Control structure

are arbitrary small constants and $e_0(t), e_1(t), e_2(t)$ will be bounded by these thresholds in a finite time after applying the two-stage controller, it is shown that the visual regulation task can be completed. Moreover, since $e_0(t), e_1(t)$ and $e_2(t)$ are bounded by their thresholds exponentially, the stability of the closed-loop system is called exponentially bounded stability.

4 Simulations

In this section, simulation results are provided to validate the proposed approach. We assume that the three feature points are not on the same vertical plane, and their coordinates in $\mathcal{F}_c^*$ are selected as $P_1^* = (2.5, 0, 0.5)^{\mathrm{T}}\mathrm{m}$, $P_2^* = (4, -0.2, -0.1)^{\mathrm{T}}\mathrm{m}$, $P_3^* = (4, 1, -0.2)^{\mathrm{T}}\mathrm{m}$. The intrinsic camera matrix is given by

$$K_{\mathrm{int}} = \begin{bmatrix} 1 & 0 & 0 \\ 344.41 & 712 & 0 \\ 238.08 & 0 & 707 \end{bmatrix} \tag{47}$$

which is chosen from a real calibrated camera with a resolution 640×480.

Table 3 Desired and initial image pixels of the feature points in the experiments

Image pixels	Expt. 1	Expt. 2	Expt. 3
(u_1^*, v_1^*)	(410,115)	(433,114)	(324,94)
(u_2^*, v_2^*)	(360,211)	(382,211)	(265,206)
(u_3^*, v_3^*)	(467,215)	(491,213)	(389,212)
(u_1, v_1)	(274,153)	(203,144)	(437,154)
(u_2, v_2)	(238,220)	(162,217)	(402,221)
(u_3, v_3)	(313,223)	(246,221)	(477,224)

In the simulation, the initial errors of Eqs. 15–17 are chosen as $e_0(0) = 0.524, e_1(0) = -0.866, e_2(0) = 3.5$, the extrinsic parameters are set as $L = 0.2$m, $D = 0.1$m, and the initial values of the estimation parameters $\hat{d}^*(0), \hat{\rho}(0), \hat{D}(0)$ are all set to be zero. The control gains and the update gains are selected as $k_0 = 0.5, k_1 = 0.1, k_2 = -1, k_3 = 0.45, K_b = 0.6, K_1 = 0.008, K_2 = -1.2, \Gamma_1 = 0.5, \Gamma_2 = \text{diag}\{0.3, 0.1\}$ and the thresholds are chosen as $\tau_{e0} = 0.02, \tau_{e1} = 0.02, \tau_{e2} = 0.001$.

Figure 6a and b show the evolution of the system errors and the image trajectories of the three feature points, respectively, where the pentagram and star points denote the initial and desired image of $\mathcal{P}_i$. It is shown from the figure that $e_0(t)$ and $e_1(t)$ decay quickly to a small neighborhood of zero. And after a period of overshoot, $e_2(t)$ is bounded by its threshold. The control inputs $\omega_r(t)$ and $v_r(t)$ are displayed in Fig. 6c and d, respectively, from which it can be seen that they are both bounded.

To further test the performance of the controller, different $e(0), d^*, L, D$ are considered and the specific setup details are given in Table 2. Moreover, we use the same control gains, update gains and thresholds as those of the original setting. Figure 7 displays the corresponding system errors in these cases, from which we can find that

$e(t)$ will be bounded by their thresholds in a finite time. These simulation results demonstrate the robustness of the proposed two-stage controller and the parameter tuning is much simple since it only requires the control gains to satisfy the condition (28).

5 Experiments

Experiments are conducted on a vision-based robot system shown in Fig. 3. The system is composed of a WMR and a HP HD 3310 camera with a resolution of 640×480 pixels. The WMR is developed in the lab, having size of 150 cm $\times$ 55 cm $\times$ 55 cm and it is equipped with two driving wheels and two supporting wheels. The wheels of radius (r) of 6.4 cm are separately mounted on a chassis of length $(2b)$ 45 cm. Each driving wheel is driven by the equipped DC motor with rated torque 72.1 mNm/A at 5200 rpm. To get the motion data and reduce the speeds to the desired ones, an incremental encoder counting 2048 pulses/turn and a drive gear with a reduction of 85.33 are equipped on each motor.

To facilitate the image processing, three artificial circle blue features are printed and attached on a plane surface. The functions of the OpenCV library including image

Fig. 9 Experiment 1: **a** System errors e; **b** Robot position (x_{rw}, y_{rw}); **c** Pixels of $\mathcal{P}_i$; **d** Control input (v_r, ω_r)
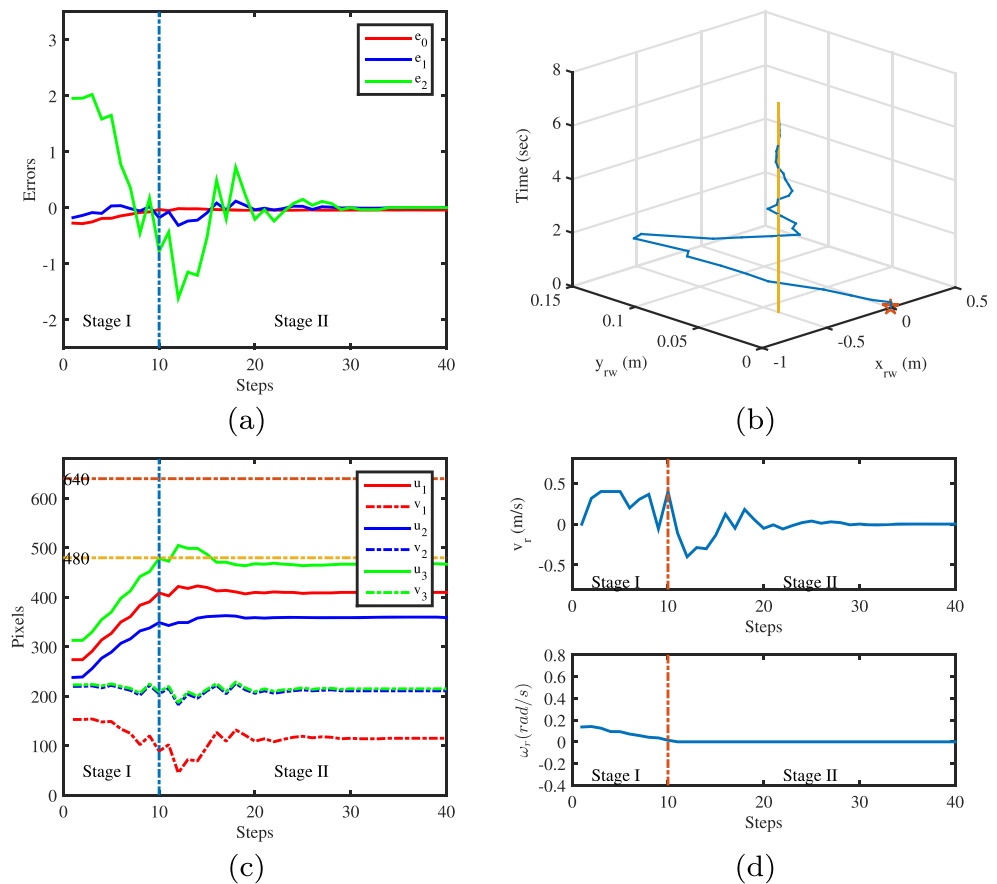
reading, denoising, binarization, and the contour finding, are utilized to extract the features. In this way, their centers (feature points) can be calculated. With the pose estimation technique based on the feature points, the regulation errors e_0, e_1, e_2 are estimated in real time. After obtaining these values, the linear and angular velocities of the WMR are computed first by the proposed two-stage controller, and then they are converted into the angular velocity commands of the left and right wheels by $\omega_L = \frac{v_r - \omega_r b}{r}$, $\omega_R = \frac{v_r + \omega_r b}{r}$. The control scheme is written in C++ language under Visual Studio 2005 environment on the host computer.

The two-layer control structure of the WMR is shown in Fig. 8. The proposed two-stage controller serves as the high level control layer, which is used to generate the velocity commands. The built-in Elmo driver controller constitutes the low level controller, which firstly gets the velocity commands from the high level control layer through CAN bus and obtains the counts data from the encoders, then generate the computed input torques to drive the motors.

Before applying the proposed two-stage controller to the WMRs, the orientation of camera is adjusted to be coincident with $\mathcal{F}_r^*$. Then three experiments are conducted with the same control parameters: $k_0 = 0.5$, $k_1 = 1.5$, $k_2 = $

-2.6, $k_3 = 0.25$, $K_b = 2$, $K_1 = 0.06$, $K_2 = -10.4$, $\Gamma_1 = 0.249$, $\Gamma_2 = \text{diag}\{0.2, 0.25\}$, $\tau_{e0} = 0.053$, $\tau_{e1} = 0.08$. The initial values of the estimated parameters $\hat{d}^*(0)$, $\hat{\rho}(0)$, $\hat{D}(0)$ are also set as zero, and the sampling time of the system is $T = 200$ ms. With the purpose to limit the frequency of the wheel-slip during the visual servoing process, saturation constraints are imposed on the velocities of the WMR, and the maximum velocities are set as: $v_{r,max} = 0.4$ m/s, $\omega_{r,max} = 1$ rad/s. The initial and desired image pixels of $\mathcal{P}_1, \mathcal{P}_2, \mathcal{P}_3$ are listed in Table 3.

The experimental outcomes can be seen from Figs. 9, 10 and 11. In the first and second experiments, the initial and desired postures of the WMRs are different, and the initial angular errors $e_0(0)$ are both negative. Figures 9a and 10a show the evolvements of the system errors during the visual servoing process: at the end of Stage I, $e_0(t)$ and $e_1(t)$ are reaching to their thresholds, and then $e_2(t)$ decays exponentially to a small neighborhood of zero in Stage II. Figures 9b and 10b depict the motion path of the robot. The corresponding image pixels of the three feature points are shown in Figs. 9c and 10c, respectively. It is obvious that the current pixels almost converge to their ideal ones. The control signals $v_r(t)$ and $\omega_r(t)$ are presented in Figs. 9d

Fig. 10 Experiment 2: **a** System errors e; **b** Robot position (x_{rw}, y_{rw}); **c** Pixels of $\mathcal{P}_i$; **d** Control input (v_r, ω_r)
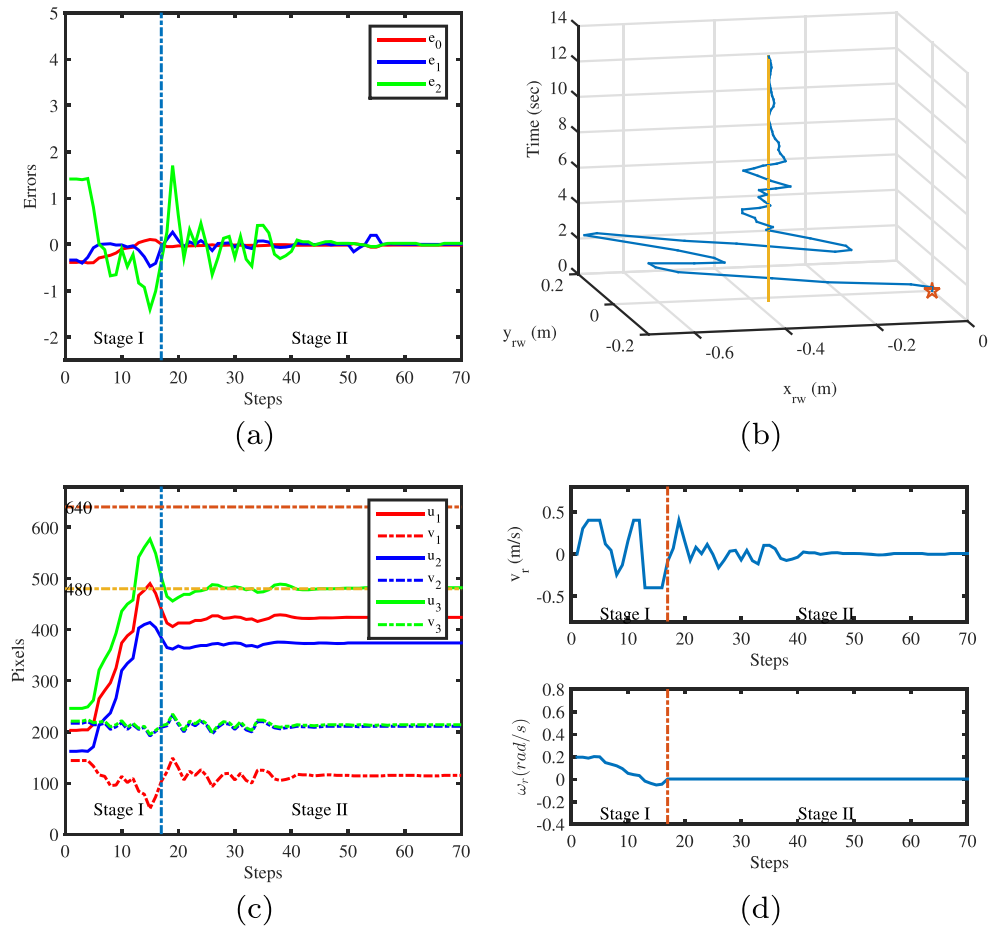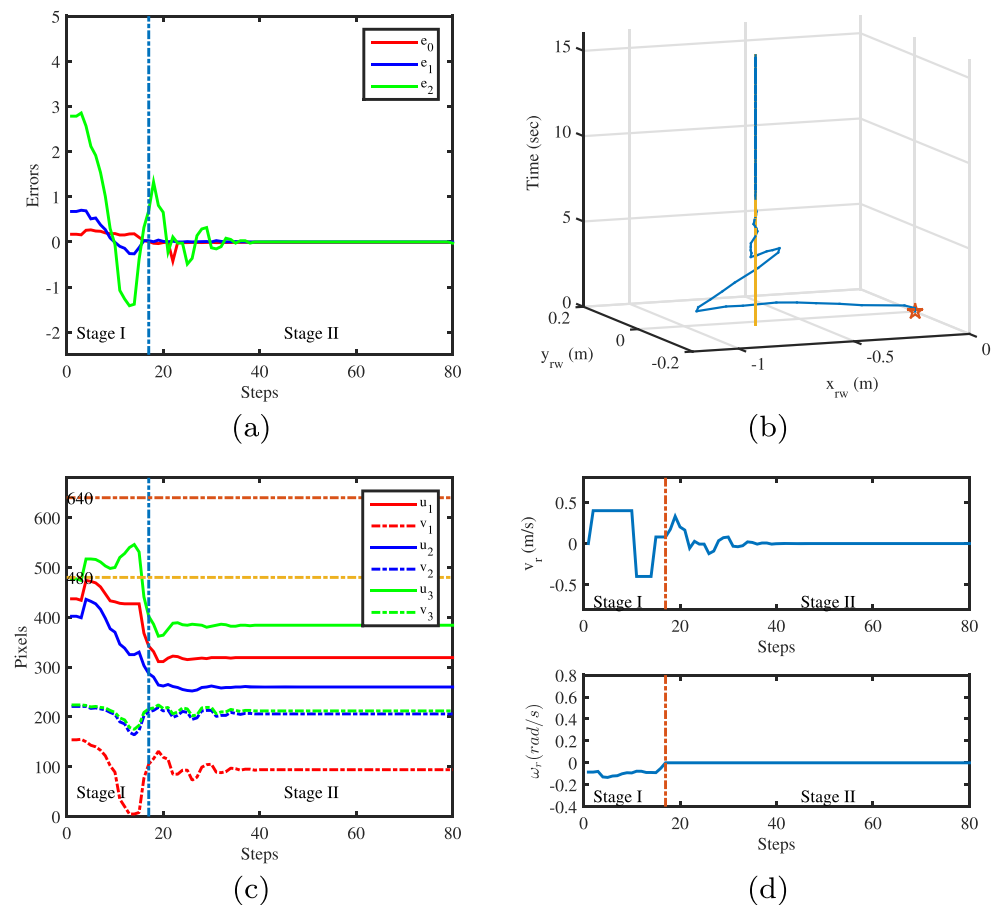
Fig. 11 Experiment 3: **a** System errors e; **b** Robot position (x_{rw}, y_{rw}); **c** Pixels of $\mathcal{P}_i$; **d** Control input (v_r, ω_r)

(a)

(b)

(c)

(d)

and 10d, from which we can find that $\omega_r(t)$ and $v_r(t)$ are both bounded.

In the third experiment, the initial angular error is positive. It can be seen from Fig. 11c that the feature point $\mathcal{P}_1$ has escaped from the camera FOV during the visual servoing process. However, the error signals can still be reconstructed by using the feature-point-based estimation technique [12]. Figure 11a and c show that $e(t)$ are bounded by their thresholds in a finite time and the current image pixels almost converge to the desired ones. Figure 11b and d show the motion path and the control inputs of the WMR in the third experiment, respectively. Different from the simulations, the chatter phenomenon observed in the experiments is shown in Figs. 9–11. The main reason is because of the image noises as well as the vibration images caused by camera shake.

6 Conclusion

This paper has investigated the problem of realizing visual servoing for a class of nonholonomic wheeled mobile robots in the presence of both uncalibrated camera-to-robot parameters and unknown image depth. By utilizing the

feature-point-based pose estimation technique, the relative error between the current and desired configurations of a WMR was firstly estimated. Then, a novel adaptive two-stage switching approach was proposed to stabilize the visual servoing system in terms of the relative error. Finally, both simulations and experiments were performed to substantiate the effectiveness of the proposed control scheme. In the future, new solutions will be explored for the uncalibrated camera-to-robot rotation angles.

References

1. David, A., Jean, P.: Computer Vision: a Modern Approach. Prentice–Hall Inc., Upper Saddle (2012)
2. Bonin-Font, F., Ortiz, A., Oliver, G.: Visual navigation for mobile robots: a survey. J. Intell. Robot. Syst. **53**(3), 263–296 (2008)
3. Yang, C., Wu, H., Li, Z., He, W., Wang, N., Su, C.-Y.: Mind control of a robotic arm with visual fusion technology. IEEE Trans. Ind. Inf. **14**(9), 3822–3830 (2018)
4. He, W., Li, Z., Philip Chen, C.L.: A survey of human-centered intelligent robots: issues and challenges. IEEE/CAA J. Autom. Sinica **4**(4), 602–609 (2017)
5. Chaumette, F., Hutchinson, S.: Visual servo control part I: basic approaches. IEEE Robot. Autom. Mag. **13**(4), 82–90 (2006)
6. Hutchinson, S., Hager, G.D., Corke, P.I.: A tutorial on visual servo control. IEEE Trans. Robot. Autom. **12**(5), 651–670 (1996)

7. Fang, Y., Liu, X., Zhang, X.: Adaptive active visual servoing of nonholonomic mobile robots. IEEE Trans. Ind. Electron. **59**(1), 486–497 (2012)

8. Wang, C., Liang, Z., Liu, Y.: Dynamic feedback robust regulation of nonholonomic mobile robots. In: Proceedings IEEE International Conference on Decision Control, pp. 4384–4389 (2009)

9. Li, B., Fang, Y., Zhang, X.: Visual servo regulation of wheeled mobile robots with an uncalibrated onboard camera. IEEE/ASME Trans. Mechatron. **21**(5), 2330–2342 (2016)

10. Lópezfranco, M., Sanchez, E., Alanis, A., Lópezfranco, C.: Discrete time neural control of a nonholonomic mobile robot integrating stereo vision feedback. In: Proceedings of the International Joint Conference on Neural Networks, pp. 4–9 (2013)

11. Vidal, R., Shakernia, Q., Sastry, S.: Following the flock: distributed formation control with omnidirectional vision-based motion segmentation and visual servoing. IEEE Robot. Autom. Mag. **11**, 14–20 (2004)

12. Zhang, X., Fang, Y., Liu, X.: Motion-estimation-based visual servoing of nonholonomic mobile robots. IEEE Trans. Robot. **27**(6), 1167–1175 (2011)

13. Louchene, A., Bouguechal, N.E.: Indoor mobile robot local path planner with trajectory tracking. J. Intell. Robot. Syst. **37**(2), 163–175 (2003)

14. Wang, H., Guo, D., Liang, X., Chen, X., Hu, W., Leang, K.K.: Adaptive vision-based leader-follower formation control of mobile robots. IEEE Trans. Ind. Electron. **64**(4), 2893–2902 (2017)

15. Chen, J., Jia, B., Zhang, K.: Trifocal tensor-based adaptive visual trajectory tracking control of mobile robots. IEEE Trans. Cybern. **47**(11) (2017)

16. Wang, G., Wang, C., Du, Q.: Robust regulation of mobile robots with dynamic based on uncalibrated visual servoing. In: Proceedings of the 11th WCICA, pp. 267–272 (2014)

17. Mariottini, G.L., Oriolo, G., Prattichizzo, D.: Image-based visual servoing for nonholonomic mobile robots using epipolar geometry. IEEE Trans. Robot. **23**(1), 87–100 (2007)

18. De Luca, A., Oriolo, G., Giordano, P.R.: Feature depth observation for image-based visual servoing: theory and experiments. Int. J. Robot. Res. **27**(10), 1093–1116 (2008)

19. Carvalho, E., Silva, M.P., Cardeira, C.: Decentralized formation control of autonomous mobile robots. In: Proceedings, 35th Annual IEEE IECON, pp. 1504–1509 (2009)

20. Malis, E., Chaumette, F., Boudet, S.: 2 1/2 D visual servoing. IEEE Trans. Robot. Autom. **15**(2), 238–250 (1999)

21. Fang, Y., Dixon, W., Dawson, D., Chawda, P.: Homography-based visual servo regulation of mobile robots. IEEE Trans. Syst. Man Cybern. B: Cybern. **35**(5), 1041–1050 (2005)

22. Li, B., Fang, Y., Hu, G., Zhang, X.: Model-free unified tracking and regulation visual servoing of wheeled mobile robots. IEEE Trans. Control Syst. Technol. **24**(4), 1328–1339 (2016)

23. Ke, F., Li, Z., Xiao, H., Zhang, X.: Visual servoing of constrained mobile robots based on model predictive control. IEEE Trans. Syst. Man Cybern: Syst. **47**(7), 1428–1438 (2017)

24. Chen, H., Zhang, J., Chen, B., Li, B.: Global practical stabilization for non-holonomic mobile robots with uncalibrated visual parameters by using a switching controller. IMA J. Math. Control **30**(4), 543–557 (2013)

25. Lu, Q., Yu, L., Zhang, D., Su, C.: An extended immersion and invariance for acceleration-level pseudo-dynamic visual regulation of mobile robots. In: Proceedings of the IEEE Control and Automation Conference, pp. 1180–1185 (2018)

26. Sun, K., Mou, S., Qiu, J., Wang, T., Gao, H.: Adaptive fuzzy control for non-triangular structural stochastic switched nonlinear systems with full state constraints. IEEE Trans. Fuzzy Syst. https://doi.org/10.1109/TFUZZ.2018.2883374

27. Zhang, X., Fang, Y., Li, B., Wang, J.: Visual servoing of nonholonomic mobile robots with uncalibrated camera-to-robot parameters. IEEE Trans. Ind. Electron. **64**(1), 390–400 (2017)

28. Zhang, X., Fang, Y., Liu, X.: Adaptive visual servo regulation of mobile robots. Control Theory Appl. **27**(9), 1123–1130 (2010)

29. Lu, Q., Yu, L., Zhang, D., Zhang, X.: Simultaneous tracking and regulation visual servoing of wheeled mobile robots with uncalibrated extrinsic parameters. Int. J. Syst. Sci. **49**(1), 217–229 (2018)

30. Tayebi, A., Rachid, A.: Adaptive controller for non-holonomic mobile robots with matched uncertainties. Adv. Robot. **14**(2), 105–118 (2000)

31. De Wit, C.C., Khennouf, H.: Quasi-continuous stabilizing controllers for nonholonomic systems: Design and robustness consideration. In: Proceedings of 3rd ECC, pp. 2630–2635 (1995)

32. Reyhanoglu, M.: On the stabilization of a class of nonholonomic systems using invariant manifold technique. In: Proceedings of the 34th IEEE Conference on Decision and Control, pp. 2125–2126 (1995)

33. Tayebi, A., Tadjine, M., Rachid, A.: Invariant manifold approach for the stabilization of nonholonomic chained systems: application to mobile robots. Nonlinear Dyn. **24**(2), 167–181 (2001)

34. Tayebi, A., Tasjine, M., Rachid, A.: Stabilization of nonholonomic systems in chained form: application to a car-like mobile robot. In: Proceedings of the IEEE International Conference on Control Applications, pp. 195–200 (1997)

35. Yoshimura, S., Watanabe, K., Maeyama, S.: Quasi-continuous exponential stabilization for the underactuated control of a fire truck robot by using an invariant manifold theory. In: Proceedings of the IEEE International Conference on Mechatronics and Automation, pp. 692–697 (2013)

36. Li, S., Ma, G., Wu, W.: Time-varying adaptive stabilization of an uncertain nonholonomic moible robots. Robot **27**(1), 10–13 (2005)

37. Zhang, W., Yang, X., Yu, L., Liu, S.: Sequential fusion estimation for RSS-based mobile robots localization with event-driven WSN. IEEE Trans. Ind. Inf. **12**(4), 1519–1528 (2016)

38. Tsalatsanis, A., Valavanis, K., Tsourveloudis, N.: Mobile robot navigation using sonar and range measurements from uncalibrated cameras. J. Intell. Robot. Syst. **48**(2), 253–284 (2007)

39. Li, Z., Deng, J., Lu, R., Xu, Y., Bai, J., Su, C.-Y.: Trajectory tracking control of mobile robot systems incorporating neural-dynamic optimized model predictive approach. IEEE Trans. SMC: Syst. **46**(6), 740–749 (2016)

40. Zhang, Z.: A flexible new technique for camera calibration. IEEE Trans. Pattern Anal. Mach. Intell. **22**(11), 1330–1334 (2000)

41. Slotine, J., Li, W.: Applied Nonlinear Control. Printice-Hall Inc., Englewood Cliffs (1991)

Qun Lu received the B.Eng. degree in mechatronics from Yancheng Institute of Technology, Yancheng, China, in 2011, and the Ph.D. degree in control science and engineering from Zhejiang University of Technology, Hangzhou, China, in 2018. He is currently a Research Intern with the Department of Mechanical, Industrial, and Aerospace Engineering, Concordia University, Quebec, Canada. He is also a Lecturer with the College of Electrical Engineering, Yancheng Institute of Technology, Yancheng, China. Dr. Lu's current research interests include adaptive control and visual servoing of mobile robots.

Zhijun Li received the Ph.D. degree in mechatronics, Shanghai Jiao Tong University, P. R. China, in 2002. From 2003 to 2005, he was a Postdoctoral Fellow in Department of Mechanical Engineering and Intelligent systems, The University of Electro-Communications, Tokyo, Japan. From 2005 to 2006, he was a Research Fellow in the Department of Electrical and Computer Engineering, National University of Singapore, and Nanyang Technological University, Singapore. Since 2012, he was a Professor in College of Automation Science and Engineering, South China university of Technology, Guangzhou, China. From 2017, he is a Professor in Department of Automation, University of Science and Technology, Hefei, China.

From 2016, he has been the Co-Chairs of Technical Committee on Bio-mechatronics and Bio-robotics Systems, IEEE Systems, Man and Cybernetics Society, and Technical Committee on Neuro-Robotics Systems, IEEE Robotics and Automation Society. He is serving as an Editor-at-large of Journal of Intelligent & Robotic Systems, and Associate Editors of several IEEE Transactions. Dr. Li's current research interests include service robotics, tele-operation systems, nonlinear control, neural network optimization, etc.

Li Yu received the B.S. degree in control theory from Nankai University, Tianjin, China, in 1982, and the M.S. and Ph.D. degrees in control theory from Zhejiang University, Hangzhou, China. Currently, he is a Professor with the College of Information Engineering, Zhejiang University. He has authored or co-authored three books and over 200 journal or conference papers. Dr. Yu's research interests include wireless sensor networks, networked control systems, and motion control.

Chun-Yi Su received the Ph.D. degree in control engineering from the South China University of Technology, Guangzhou, China, in 1990. He joined Concordia University, Montreal, QC, Canada, in 1998, after a seven-year stint with the University of Victoria, Victoria, BC, Canada. He is currently a Professor with the School of Automation, Guangdong University of Technology, on leave from Concordia University. He has authored or co-authored over 400 publications in journals, book chapters, and conference proceedings. Dr. Su's research interests include the application of automatic control theory to mechanical systems, in particular, the control of systems involving hysteresis nonlinearities. Dr. Su has served as an Associate Editor of the IEEE Transactions on Automatic Control and the IEEE Transactions on Control Systems Technology. He has been on the Editorial Board of many journals, including the IFAC Journal of Control Engineering Practice and Mechatronics. He served for many conferences as an Organizing Committee Member, including the General Chairs and Program Chairs.